Applied Catalysis B: Environmental 144 (2014) 277–285

Contents lists available at ScienceDirect

Applied Catalysis B: Environmental

journal homepage: www.elsevier.com/locate/apcatb

Glycerol steam reforming over perovskite-derived nickel-based catalysts

Gaowei Wu[a,b], Shuirong Li[a,b], Chengxi Zhang[a,b], Tuo Wang[a,b], Jinlong Gong[a,b,*]

[a] Key Laboratory for Green Chemical Technology of Ministry of Education, School of Chemical Engineering and Technology, Tianjin University, Tianjin 300072, China
[b] Tianjin Co-Innovation Center of Chemical Science and Engineering, Tianjin 300072, China

ARTICLE INFO

Article history:
Received 11 May 2013
Received in revised form 8 July 2013
Accepted 11 July 2013
Available online 19 July 2013

Keywords:
Hydrogen
Ni-based catalyst
Perovskite-type oxide
Glycerol steam reforming
Metal-support interaction

ABSTRACT

This paper describes the synthesis and application of $La_{1-x}Ca_xNiO_3$ perovskite-type oxides in glycerol steam reforming. Various techniques including N_2 adsorption-desorption, X-ray diffraction, H_2 temperature-programmed reduction, temperature-programmed oxidation, H_2 chemisorption, transmission electron microscopy, and thermogravimetric analysis were used to characterize the prepared catalysts. The results showed that the perovskite structure could promote the even distribution of the containing elements (Ni, La or Ca) upon reduction, which led to the increase in the interfacial area between Ni and oxides *via* a confinement effect. Consequently, stronger metal-support interaction and smaller Ni metallic particles were observed on $LaNiO_3$, rather than Ni/La_2O_3 catalyst prepared by the impregnation method. Effects of lanthanum substitution by calcium on properties of the perovskite-type oxides were also studied. $La_{0.5}Ca_{0.5}NiO_3$ was the optimized composition for the steam reforming catalysts, owing to its strong metal-support interaction and high metal dispersion resulted from the synergetic interaction of La and Ca. Both properties were critical to the performance of glycerol steam reforming catalysts. Additionally, spent catalysts (e.g., upon 30 h stability test) were also characterized, which revealed the deactivation of catalysts was ascribed to coke deposition that covers the active sites. Specifically, smaller Ni particle size and stronger metal-support interaction could suppress carbon deposition, and thus improved the catalyst stability in glycerol steam reforming.

1. Introduction

With the diminishing reserves of fossil fuels, it is urgent to develop sustainable energy resources. Bio-diesel, derived from transesterification of vegetable oils, animal products, or waste fats, was proposed to be the substitute for diesel [1–3]. Nowadays, a large amount of crude glycerol, usually containing methanol, water and salts, are produced as the byproduct of bio-diesel (100 kg of glycerol per ton of bio-diesel) with the rapid growth of the bio-diesel industry [4–8]. To make bio-diesel economically competitive to regular diesel at the present stage, it is essential to develop technologies to improve the utilization of crude glycerol. However, the main and traditional applications of glycerol (food additives, health care and pharmaceuticals) are significantly restricted to low-quality glycerol unless an energy-intensitive purification step is previously carried out [1,4,9]. Among those other markets for which crude glycerol may be directly utilized, the use of this resource as a source of hydrogen provides a possible solution for the dilemma, especially in the case of large-scale production [2,5,10,11].

Hydrogen is widely used in the chemical and petroleum industries, as well as identified as a promising clean energy for electrical power generation and fuel cell devices [12]. H_2 used in current industries is primarily produced from steam reforming of natural gas, during which a large amount of CO_2 was discharged [13]. However, it is deemed as a carbon-neutral process to utilize the renewable glycerol. Therefore, the production of hydrogen from renewable glycerol could contribute to the reduction of greenhouse gases and the sustainable development of modern economy [10,13–15].

$$C_3H_8O_3 + 3H_2O \leftrightarrow 7H_2 + 3CO_2 \quad \Delta H_{298\,K} = +128\ \text{kJ/mol} \tag{1}$$

Various types of catalytic conversion systems such as pyrolysis, [16] partial oxidation and autothermal reforming [17,18], aqueous phase reforming [19,20], and steam reforming [21–24] have been investigated to convert glycerol to hydrogen and have been extensively discussed in previous work (see reviews [25–27]). Among these processes, glycerol steam reforming (GSR, Eq. (1)) is the most common one due to its ambient pressure reaction condition and high selectivity compared to aqueous phase reforming [28,29].

* Corresponding author. Tel.: +86 22 87401818; fax: +86 22 87401818.
E-mail address: jlgong@tju.edu.cn (J. Gong).

0926-3373/$ – see front matter © 2013 Elsevier B.V. All rights reserved.
http://dx.doi.org/10.1016/j.apcatb.2013.07.028

Though usually operated at relatively high temperatures (e.g., above 400 °C), this endothermic process could also be compensated by other exothermic ones (e.g., Fischer–Tropsch, methanol syntheses) to realize an available energy-efficient route for the H_2 production [10,14]. Nickel-based catalysts have been commercialized for industrial steam reforming processes including GSR in laboratory scale [27,30,31]. At present, carbon deposition and metal sintering are the major challenges for designing GSR catalysts [27]. As reported in previous work, nickel particle size and metal-support interaction (MSI) had significant effects on the performance of GSR catalysts [22,31,32], and our previous work also proved that these properties could be modified by the synthesis of a certain particular structure (e.g., hydrotalcite-like structure, phyllosilicate structure and inset of metal particle in the frame of the oxides) [33–35].

Recently, perovskite-type oxides have received increasing attention worldwide in steam reforming process due to its special crystal structure [36,37,21,38,39]. Perovskites are mixed oxides with a general formula of ABO_3, where A is an alkali, alkaline earth or rare earth metal and B is usually an element in the transition series [40,41]. Both A and B can be partially substituted with a great range of metal cations within the size constraints of the A and B sites, leading to a wide variety of compounds with modified catalytic, redox and structural properties [42]. These mixed oxides with well-defined cubic structure are capable of producing well-dispersed metallic particles upon reduction treatment [43–45]. Thus, the catalysts derived from perovskite-type oxides could avoid carbon formation, and present superior catalytic activity and stability [43,46]. Among these suitable perovskite-type oxides for reforming reaction, $LaNiO_3$ was widely studied due to its high catalytic activity [43,44,47,48]. Additionally, the effect of partial substitution of La by other metal (Ce, Ca, Sr, Sm, Nd, etc.) was also investigated in order to introduce the structural and electronic defects or enhance the interaction with B-site metal, which helped achieve highly active and stable catalysts [36,39,49,50].

Among these substitution elements, as a well-known alkaline earth metal, Ca has been used as a catalyst promoter in various kinds of reactions (e.g. methane dry reforming [51], ethanol steam reforming [52], oxidative steam reforming of glycerol [53]). The calcium dopant has been proved to generate positive catalytic effect in terms of higher activity and stability. However, the information about the performance of perovskite-type oxides, as well as the substitution of La by Ca, in GSR is limited [21]. Therefore, this paper describes a detailed investigation regarding the application of $La_{1-x}Ca_xNiO_3$ (x = 0.0, 0.1, 0.3, 0.5, 0.7 and 1.0) in GSR. Various techniques including N_2 adsorption-desorption, X-ray diffraction (XRD), H_2 temperature-programmed reduction (TPR), H_2 chemisorption, temperature-programmed oxidation (TPO), transmission electron microscopy (TEM), and thermogravimetric analysis (TGA) were performed to characterize the prepared catalysts. The catalytic performance of the derived nickel-based catalysts in GSR was investigated and compared with a reference Ni/La_2O_3 catalyst.

2. Experimental

2.1. Catalyst preparation

The $La_{1-x}Ca_xNiO_3$ perovskite-type oxides used in this study were prepared by decomposition of amorphous citrate as described previously [36,54]. $Ni(NO_3)_2{\bullet}6H_2O$ (98.0%, Shanghai Chemical Reagent Company of National Medicine Group), $Ca(NO_3)_2{\bullet}4H_2O$ (98.0%, Shanghai Chemical Reagent Company of National Medicine Group) and $La(NO_3)_3{\bullet}6H_2O$ (98.0%, Tianjin Jierzheng Chemical Co., Ltd.) with desired molar ratios were dissolved in deionized water. Then, a concentrated solution of citric acid (98.0%, Tianjin No.1 Chemical Reagent Factory) with 20% excess over the total molars of cations was prepared and added to the nitrate solution. The resulting solution was heated to 60 °C and kept at this temperature for 9 h, followed by evaporating for 0.5 h using a vacuum rotary evaporator. The viscous solution was then dried at 120 °C for 12 h, which resulted in a spongy solid. The resultant solids were grinded and calcined in two stages: first at 300 °C for 2 h and then at 800 °C for 5 h, to obtain the final perovskite structure. Though not all the samples present perovskite structure, the nomenclature $La_{1-x}Ca_xNiO_3$ is used in all cases for uniformity and labeled as LCx (x = 0.0, 0.1, 0.3, 0.5, 0.7 and 1.0) [36].

A reference Ni/La_2O_3 catalyst containing the same Ni content as LC0.0 was also prepared by the impregnation method. The La_2O_3 support was first obtained by calcining the lanthanum nitrate at 800 °C, and then impregnated in a $Ni(NO_3)_2$ solution by mechanical agitation at 60 °C for 9 h, followed by evaporation at 60 °C using a vacuum rotary evaporation until the water was removed. The resultant solid was dried at 120 °C for 12 h, and then calcined at 800 °C for 5 h.

2.2. Physical characterization

XRD measurements were performed with 2θ values between 10 and 85° by using a Rigaku C/max-2500 diffractometer employing the graphite filtered Cu Kα radiation (λ = 1.5406 Å). The Scherrer equation was used to estimate the mean Ni crystallite size based on the diffraction peaks of the Ni (1 1 1) facet.

Textual properties of the catalysts were measured with a Micromeritics Tristar 3000 analyzer by nitrogen adsorption at −196 °C. The samples were degassed at 300 °C for 4 h prior to measurements. This instrument employed the Brunauer–Emmett–Teller (BET) method by measuring the quantity of nitrogen absorbed at −196 °C and the cumulative volumes of pores were obtained by the Barrett–Joyner–Halenda (BJH) method from the desorption branches of the adsorption isotherms.

H_2-TPR was employed to analyze the reduction behavior of the catalysts by using a Micromeritics AutoChem 2920 apparatus. A powered sample (50 mg) was pretreated at 700 °C for 1 h under flowing Ar (30 ml min^{-1}). Upon cooling to 50 °C, a flow rate of 30 ml min^{-1} of 10 vol% H_2/Ar was used for the reduction and the temperature was increased linearly from 50 to 800 °C at 10 °C min^{-1}.

TPO was carried out by using a Micromeritics AutoChem 2920 apparatus equipped with a HIDEN QIC-20 mass spectrometer (MS). The spent catalyst (20 mg) was pretreated at 800 °C for 1 h under flowing Ar (30 ml min^{-1}). Upon cooling to 100 °C, a flow rate of 30 ml min^{-1} of air was used for the oxidation and the temperature was increased linearly from 100 to 750 °C at 10 °C min^{-1}. The CO_2 in the effluent was monitored and recorded online by MS.

The quantitative content of Ni in prepared samples was measured by inductively coupled plasma optical emission spectroscopy (ICP-OES) (VISTA-MPX, Virian). Prior to measurements, the samples were digested in HCl and HNO_3 aqueous solution assisted by microwave (Multiwave 3000, Anton Paar).

Dispersion of nickel was studied by employing H_2 chemisorption. For each run, 200 mg of catalyst were pre-reduced with 10 vol% H_2/Ar at 650 °C for 1 h, and then flushed with Ar at 650 °C for 30 min. H_2 chemisorption was carried out at 50 °C by injection pulses of 10 vol% H_2/Ar (0.5082 mL) every 4 min until the consumption peaks became stable (about 10 pulses).

TEM was conducted to characterize the morphology of catalysts employing a JEM-2100F transmission electron microscope at 200 kV. The microscope was also equipped with a liquid nitrogen cooled energy-dispersive X-ray spectroscopy (EDS) detector for elemental analysis. The sample was first dispersed in ethanol and

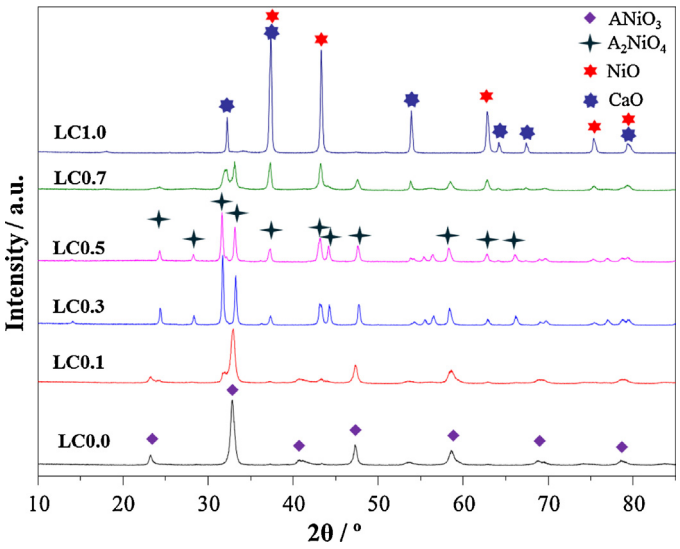

Fig. 1. XRD patterns of the $La_{1-x}Ca_xNiO_3$ perovskite-type oxides.

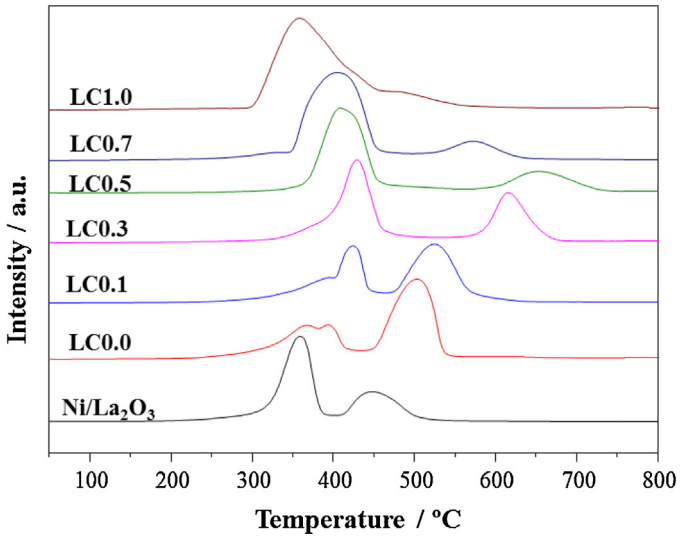

Fig. 2. H_2-TPR profiles of the $La_{1-x}Ca_xNiO_3$ perovskite-type oxides and Ni/La_2O_3.

supported on lacey-formvar carbon on a 200-mesh Cu grid before TEM images were recorded.

TGA (STA449F3 NETZSCH Corp.) was used to investigate the carbon deposition of spent catalysts. The sample was first pre-heated at 800 °C for 30 min and cooled to room temperature in N_2 (50 ml min^{-1}). Then the sample was heated from room temperature to 750 °C at the rate of 10 °C min^{-1} in air (100 ml min^{-1}).

2.3. Catalytic tests

Catalytic tests were carried out at the atmospheric pressure in a quartz fixed-bed reactor loaded with 200 mg catalyst (20–40 mesh) mixed with 1 mL quartz particles. Before the test, the catalysts were reduced at 650 °C *in situ* for 1 h in a flow of 10 vol% H_2/N_2. The liquid solution with a certain steam-to-carbon (S/C) ratio was fed through an HPLC pump into a heated chamber (250 °C) to evaporate the solution completely in the stream of N_2 before reaction. The products were first condensed through a cooler and the incondensable gas species were analyzed online by two gas chromatographs. One is equipped with a flame ionization detector (FID) and a Porapak-Q column with N_2 as the carrier gas to analyze the organic species such as methane, ethylene, and ethane. The other one is integrated with a thermal conductivity detector (TCD) and a TDX-01 column using He as the carrier gas to monitor hydrogen, carbon dioxide, carbon monoxide, and methane. Products in the condensed liquid phase were analyzed on an Agilent 7890A gas chromatographs equipped with a DB-Wax GC column.

The performance of the catalyst is presented in terms of H_2 mol yield and C-containing gas products selectivities (Eq. (2)).

$$\%\,\text{Selectivity of}\,i = \frac{i\,\text{mol}}{\left(\sum i\,\text{spices}\right)\,\text{mol produced}} \times 100 \qquad (2)$$

where i represents CO, CO_2, CH_4, C_2H_4 and C_2H_6.

3. Results and discussion

3.1. Characterization

Diffraction patterns of as-prepared $La_{1-x}Ca_xNiO_3$ perovskite-type oxides are presented in Fig. 1. The diffraction peaks at $2\theta = 23.1°$, 32.8°, 40.6°, 47.3°, 58.4°, 69.6° and 79.1° are assigned to the $LaNiO_3$ rhombohedral phase (JCPDF: 10-0341), confirming that the preparation method used is efficient to produce the perovskite structure [36,54]. LC0.0 is also successfully synthesized containing pure $LaNiO_3$ perovskite structure. With the gradual substitution of La by Ca, the samples present significant changes in reflection peaks. Though $LaNiO_3$ perovskite structure is still the main phase presented in LC0.1, the peak intensities decrease and other additional peaks are also detected simultaneously. These additional peaks clearly appear in LC0.3, which are assigned to the characteristic peaks of La_2NiO_4 (JCPDF: 22-0712) [55]. La_2NiO_4 has a tetragonal structure, and also belongs to the family of perovskite homologues with general formula A_2BO_4[42]. We need to mention that there is no obvious reflection peak of CaO detected even when x is less than 0.7. Thus, we could deduce that Ca enters into the perovskite structure and the substituted perovskite is formed [39,56]. To make it more precise, we label $ANiO_3$ and A_2NiO_4 (A = La or Ca) instead of $LaNiO_3$ and La_2NiO_4, respectively. From $x = 0.3$, A_2NiO_4, instead of $ANiO_3$, accouts for the main phase in LC*x*. For a degree of substitution $x = 0.7$, the diffraction peak intensities of A_2NiO_4 perovskite structure are obviously weaker than LC0.5. Additionally, the characteristic peaks of CaO are detected. The separation of oxides from the main perovskite phase was also reported by previous work due to the low solubility of Ca in perovskite structure [39,49,56]. The reflections of NiO are very close to those of A_2NiO_4, and thus it is difficult to confirm the existence of NiO in synthesized samples only based on XRD patterns. However, since the molar ratio of A to Ni in prepared catalyst is 1, the detected A_2NiO_4 (A/Ni = 2) would bring about superfluous NiO existing in LC*x* ($x > 0.1$). This point could also be supported by the following TPR profiles. Additionally, when La is totally substituted by Ca, only nickel and calcium oxides are presented without the detection of perovskite structure.

Since Ni^0 crystallites are deemed as the active sites for the reforming reaction, the perovskite-type oxides need to be activated by reduction before reaction [21,49]. The reducibility of LC*x* catalysts and reference Ni/La_2O_3 catalyst was investigated by H_2-TPR, and the reduction profiles are shown in Fig. 2. The reduction process of LC0.0 with the pure $LaNiO_3$ perovskite structure presents three H_2 consumption peaks (360, 380 and 500 °C). The first two peaks are assigned to the reduction of $LaNiO_3$ to $La_4Ni_3O_{10}$, and then to La_2NiO_4[21,44]. The third broad peak corresponds to the reduction of La_2NiO_4 to Ni^0 and La_2O_3[44,55]. Notably, the main peak of LC0.0 presents obviously higher reduction temperature than Ni/La_2O_3, indicating stronger MSI [31,32]. The calcium substitution has evident influence on the reduction behavior of LC*x* samples. Though LC0.1 still presents three main reduction peaks in correspondence with its main perovskite phase, a clear shift of the

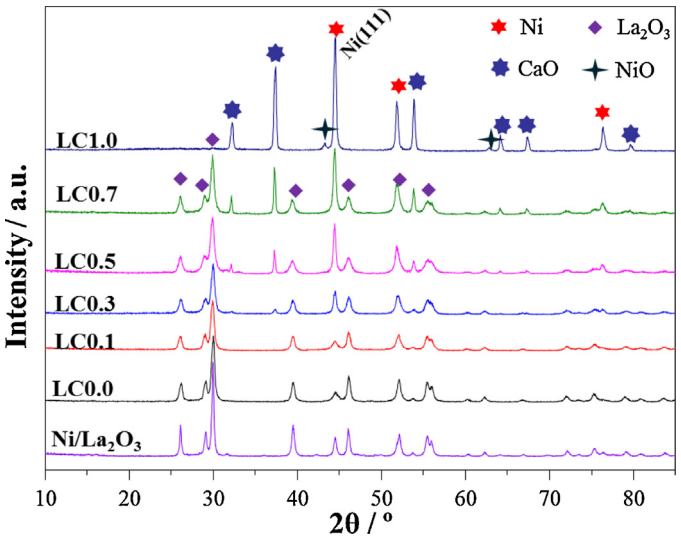

Fig. 3. XRD patterns of reduced LC*x* catalysts and Ni/La_2O_3.

peak maxima to higher temperatures is observed in the reduction profile, which also corresponds to enhance MSI. When x ranges from 0.3 to 0.7, there are only two reduction peaks occurring in the profiles of LC*x*. The high-temperature peaks at about 600 °C are attributed to the reduction of La_2NiO_4, whose temperatures are all higher than that of LC0.0. Noticeably, LC0.5 shows the highest reduction peaks among the series catalysts, which indicates the strongest interactions between Ni species and the oxides.

Since $ANiO_3$ perovskite structure is not detected in XRD patterns, the low-temperature peaks of LC*x* (x = 0.3, 0.5 and 0.7) could be only deduced to be the reduction of bulk NiO according to previous work [31,57–59]. This also proves the existence of NiO in these samples. Additionally, LC1.0 displays two reduction peaks, a broad one at 350 °C and a shoulder one at 460 °C. The former is ascribed to the reduction of bulk NiO, whose intensity agrees with that of XRD pattern, and the latter is owing to the interaction between Ni species and CaO oxide [35,52].

According to the H_2-TPR, the reduction condition of the synthesized catalysts was determined to be 650 °C for 1 h. XRD patterns of the reduced catalysts are presented in Fig. 3. After reduction treatment, the original perovskite structure is not detectable in LC*x* (x ranges from 0.0 to 0.7), but is similar to reduced Ni/La_2O_3, for which only the characteristic peaks of Ni and La_2O_3 are detected [44,49,55]. When x is higher than 0.1, the characteristic peaks of CaO are also presented in reduced LC*x*. The reduced LC1.0 contains the phases of Ni and CaO, together with small amount of unreduced NiO. It could be concluded that the perovskite-type oxides are completely destroyed and transformed to the combination of active Ni metal and the oxides.

The physical properties of LC*x* and Ni/La_2O_3 are presented in Table 1. The BET surface areas of the series of LC*x* catalysts are lower than 5.0 m^2/g, and this is the inherent characteristic of the perovskite-type oxides [36]. Additionally, the calcination at high temperature (800 °C) could also drastically reduce the specific surface area [40]. Quantitative calculations of nickel crystallite diameter based on Ni(1 1 1) facet and the Scherer equation are also shown in Table 1, together with the Ni content and the metal dispersion. It can be observed that LC0.0 derived from perovskite-type oxides presents smaller nickel particle size and higher metal dispersion than Ni/La_2O_3 prepared by the impregnation method, even though their Ni contents are the same and Ni/La_2O_3 shows larger surface area. This result reveals that the perovskite structure could produce and stabilize smaller nickel particles during the reduction process [60]. For LC*x* catalysts, the particle size of Ni, as well as the Ni content, increases gradually with the increase of x. The partially substitution of La by Ca also significantly affects the metal dispersion, and it presents an upward trend with x increasing from 0.0 to 0.5, and then decreases for x equals to 0.5 and 0.7.

3.2. Catalytic performance

The catalytic performance of LC*x* catalysts was initially investigated at 550 °C with S/C = 3 according to thermodynamic and experimental analysis for GSR [21,61,62]. Glycerol was completely converted under the selected test condition on all the samples, in agreement with previous work [21,63]. The liquid products detected in the condensed phase were mainly trace amounts of acetaldehyde, methanol, ethanol, propanal, acetone, allyl alcohol, 1-hydroxy-2-propanone, and 1, 2-propandiol. Therefore, only hydrogen molar yield and selectivities of C-containing gas products at steady stage of the reaction are shown in Fig. 4 to screen LC*x* catalysts [21,62,64,65].

Fig. 4 indicates that LC0.0 catalyst presents similar catalytic reactivity with Ni/La_2O_3. However, the LC*x* catalysts with different degree of substitution perform significantly differences in GSR. The H_2 molar yield slightly rises for LC0.1, and then dramatically increases upon the increment of Ca content. Notably, LC0.5 possesses the highest H_2 yield, reaching 5.8 mol H_2/mol glycerol, which is slightly lower than the equilibrium calculation of hydrogen (about 6.1 mol) reported by Chen et al. [66] Additionally, it presents a decreasing trend for LC0.7, and LC1.0 shows the lowest H_2 yield among the series of catalysts. The same variations of the prepared samples are also observed for CO_2 selectivity in the reaction products. Higher CO_2 selectivity generally corresponds to lower CO selectivity, thus the higher CO_2/CO ratio could be observed, which is usually deemed as the criterion for determining activity of water gas shift reaction (WGSR, Eq. (3)) [14,32,67]. Hence, the variation tendency of WGSR activity of catalysts agrees well with that of the H_2 yield, and this in turn proves that WGSR has important influence on the product distributions [13,62]. No obvious difference was

Table 1
Characterization of prepared catalysts.

Samples	Surface area (BET)/m^2/g	Average pore diameter/nm	Pore volume/cm^3/g	Particle size of Ni[a]/nm	Ni content[b]/wt%	CaO content[b]/wt%	La_2O_3 content[b]/wt%	Metal dispersion[c]/m^2/g_{cat}
Ni/La_2O_3	8.7	32.0	0.04	26.6	23.4	0.0	76.6	0.13
LC0.0	1.1	66.8	0.01	10.4	23.8	0.0	76.2	0.15
LC0.1	4.3	41.8	0.04	11.0	24.7	3.5	71.8	0.19
LC0.3	2.1	33.7	001	25.1	27.1	10.6	62.3	0.20
LC0.5	2.9	45.1	0.02	29.3	30.3	19.3	50.4	0.38
LC0.7	4.6	42.9	0.04	31.6	33.1	28.9	38.0	0.16
LC1.0	3.0	50.3	0.02	30.6	44.9	55.1	0.0	0.05

[a] Determined by the Scherrer's equation.
[b] Determined by ICP-OES.
[c] Determined by H_2 chemisorption.

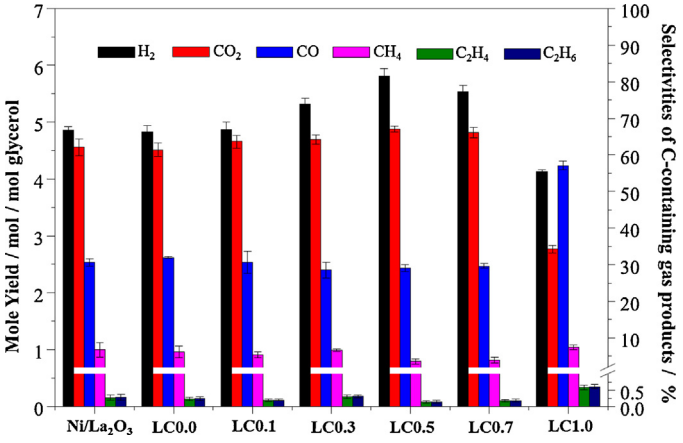

Fig. 4. H_2 mole yield and selectivities of C-containing gas products of Ni/La_2O_3 and LC*x* catalysts in GSR (Reaction condition: $T = 550\,^{\circ}C$, S/C = 3, WHSV = 2.5 h^{-1} and atmospheric pressure).

observed for the CH_4 selectivities due to the high Ni loading and the selected temperature [68]. Negligible selectivities of C_2H_4 and C_2H_6 are also attained over the synthesized catalysts, except for LC1.0. Combined with the characterization results, we could conclude that the trend of catalytic performance matches well with nickel metal dispersion. Indeed, the catalytic activity of GSR is highly affected by the amount of Ni sites [14,69,70]. LC0.5 with higher nickel dispersion could provide more active Ni sites, and hence delivers higher efficiency of H_2 production. Yet, not enough Ni sites could be provided by LC1.0 to cleave all the C—C bond, and hence relatively high content of C2 gas-phase products is detected in the sample.

$$CO + H_2O \leftrightarrow CO_2 + H_2 \quad \Delta H_{298K} = -41\ \text{kJ/mol} \tag{3}$$

GSR is generally considered as a severe reaction and its catalysts typically suffer from deactivation [32]. To better understand the substitution effect of La by Ca over perovskite-type catalysts in GSR, LC0.0 and LC0.5, as well as the Ni/La_2O_3 catalyst, were screened out with a 30 h stability test. Glycerol conversion remains 100% through the whole test. Fig. 5 displays the deactivation phenomena on the selected catalysts, yet the deactivation degree for different catalysts is evidently distinguishable. H_2 molar yield of Ni/La_2O_3 catalyst follows a downward trend at the initial 5 h, and then goes through a short-term steady state and drops dramatically. It finally keeps stable at the last 5 h (e.g., ~2.5 mol H_2/mol glycerol). The selectivity of CO_2 consists with H_2, corresponding to the rise of CO selectivity. No obvious changes were observed for the other C-containing gas-phase products. The catalytic behavior is apparently improved using the LC0.0 sample. Through the decline at the beginning, the H_2 yield of LC0.0 decreases gradually from 5 h to 15 h, and reduces to 3.2 mol H_2/mol glycerol eventually. Batiot-Dupeyrat et al. [44] have reported better catalytic performance on the catalysts derived from the $LaNiO_3$ perovskite-type oxides than that on Ni/La_2O_3 prepared by the impregnation in CO_2 reforming of CH_4. Among the three catalysts, the highest efficiency of H_2 production and relatively most stable catalytic performance are attained on the LC0.5 catalyst.

3.3. Characterization of spent catalysts

The stability test for spent catalysts was conducted by various techniques to understand the origin of catalyst deactivation. From Fig. 6, the characteristic peaks of $La_2O_2CO_3$ phase were observed in all the spent catalysts, due to the existence of CO_2 at the reaction condition [46,55]. Similarly, the phase of $CaCO_3$ was also detected in the spent LC0.5. The reflections of Ni ($2\theta = 44.6^{\circ}$, 51.3° and 76.1°) are very close to those of $La_2O_2CO_3$, and thus it is difficult

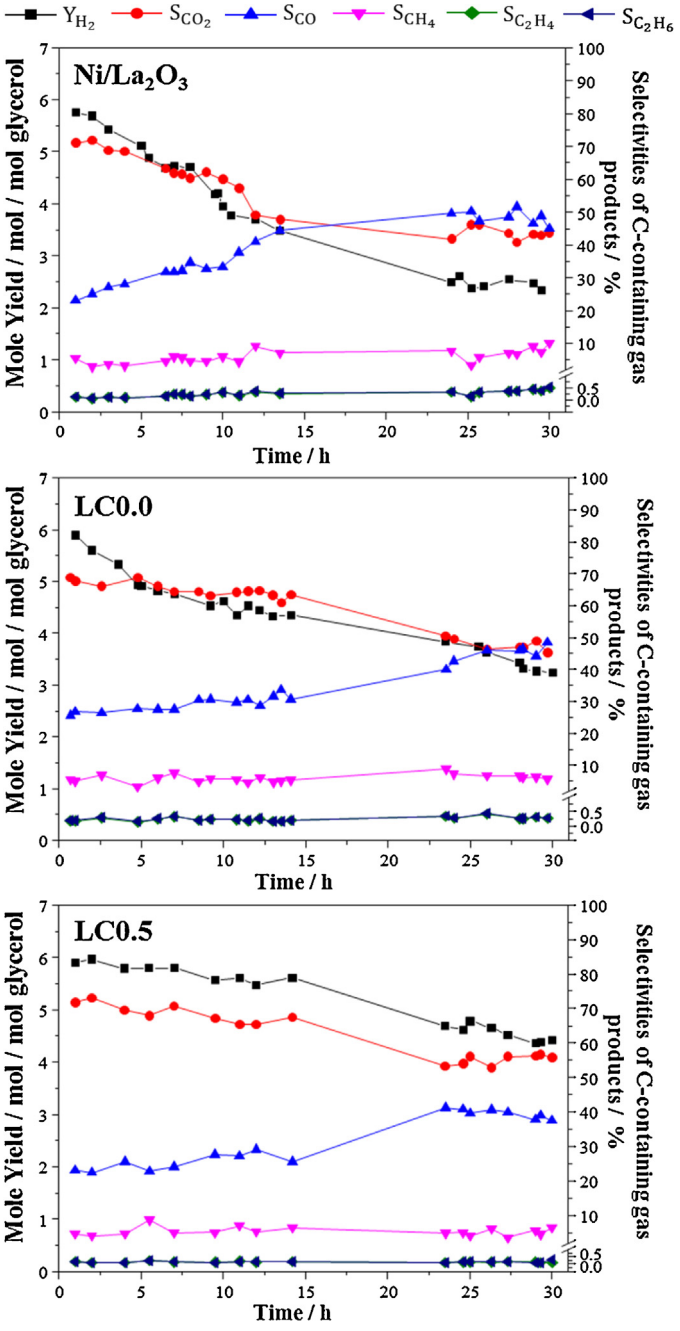

Fig. 5. Stability tests of selected catalysts in GSR (Reaction condition: $T = 550\,^{\circ}C$, S/C = 3, WHSV = 2.5 h^{-1} and atmospheric pressure).

to confirm the existence of Ni and calculate the particle size of Ni from XRD patterns. Moreover, the phase of graphite ($2\theta = 26.4^{\circ}$) was also clearly detected in spent Ni/La_2O_3.

TEM was used to examine the morphology of spent catalysts upon the stability test. It can be seen from Fig. 7a that no obvious morphology differences could be observed for the selected catalysts. To better distinguish these catalysts, STEM micrograph and EDS mapping were obtained to determine the elemental dispersion of Ni, Ca and La on the surface of prepared catalysts. From Fig. 8, the inhomogenous distribution of Ni and La was detected in Ni/La_2O_3, owing to the nature of the impregnation method. However, reduced LC0.0 catalyst derived from perovskite-type oxides presents uniform distribution of the containing elements [71,72]. Additionally, LC0.5 also shows a similar distribution, and Ni species appears to be embedded in the surrounding CaO/La_2O_3 matrix. This could also

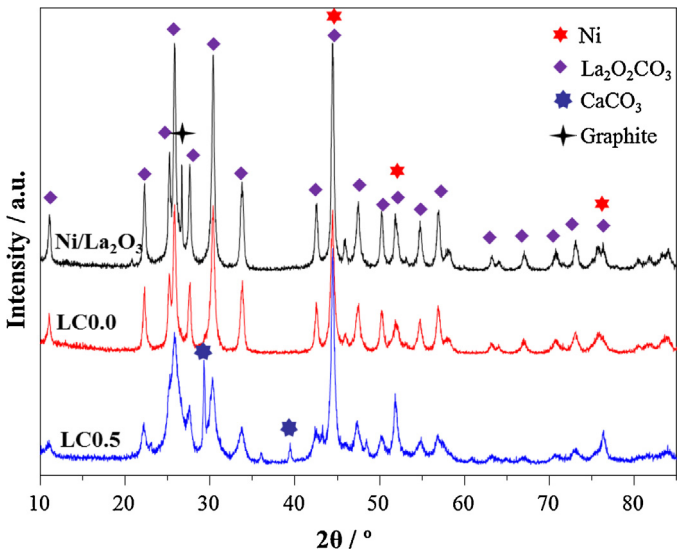

Fig. 6. XRD patterns of spent selected catalysts.

illuminate the influence of perovskite structure on the properties of LC*x* catalysts. For Ni/La_2O_3 catalyst prepared by the conventional impregnation method, nickel particles were located on the bulk La_2O_3 support, whereas the homogenous element distribution in LC*x* would increase the interfacial area, thus enhancing the MSI [34]. Additionally, the geometric confinement of the surrounding oxides could also prevent the nickel metal from sintering under high-temperature conditions [34,73,74]. Furthermore, the substitution of A-site metals with other element could possibly produce synergetic interaction with the B-site metal, [45] and LC0.5 catalyst is proved to be the optimized composition according to the characterization results.

Upon 30 h stability test, the appearance of the spent catalysts presented evident differences due to the occurrence of carbon deposition. Spent Ni/La_2O_3 catalyst was seriously encapsulated by deposited carbon, where filamentous carbon was also clearly shown in the sample [36]. This phenomenon is in accordance with XRD patterns (Fig. 6), since the phase of graphite is clearly detected in spent Ni/La_2O_3. For LC0.0, the morphology of spent catalyst did not present significant changes compared with the fresh one, and carbon deposition was not distinctly observed on the surface of the catalyst. Though carbon deposition (marked by dotted line in Fig. 7) is also noticed on LC0.5 catalyst, [75] the catalyst still remains mainly exposed.

The amount of deposited carbon was quantitatively determined by TGA, and the mass loss profiles are shown in Fig. 9. We need to mention that the spent catalysts were first pretreated at 800 °C for 0.5 h before the characterization, in order to eliminate the influence of the potential carbonate. The increase of the mass in all samples occurs from the beginning, which is caused by oxidation of the existing Ni particles. This could also confirm the existence of Ni in spent catalyst. The mass of LC0.5 rises by 7% accumulatively, obviously higher than the other two catalysts. This indicates the presence of more Ni^0 in the spent LC0.5. From Fig. 9, it can be observed that the amount of coke deposition follows the order LC0.0 (18.4%) < LC0.5 (25.4%) < Ni/La_2O_3 (37.3%). To eliminate the effect of oxidation of nickel metal, TPO was also carried out to confirm the order, and the concentration of CO_2 was detected by MS and shown in Fig. 9. The curves are normalized, and the peak area corresponds to the amount of deposited carbon. By quantifying the peak areas, we could conclude the area ratio of LC0.0, LC0.5 and Ni/La_2O_3 is 1.0:1.3:2.4. The results from TPO are consistent with that of TGA, and thus we could conclude that LC0.0 has the least amount of carbon deposition, followed by LC0.5 and Ni/La_2O_3.

Carbon deposition and active metal sintering are widely deemed as the main reasons for catalyst deactivation in GSR [27]. Though the nickel particle size of spent catalysts cannot be determined by XRD, previous studies yet pointed out that both coke formation and sintering are operative in GSR [22,27]. Coke deposition in GSR could be caused by the Boudouard reaction, as well as the polymerization

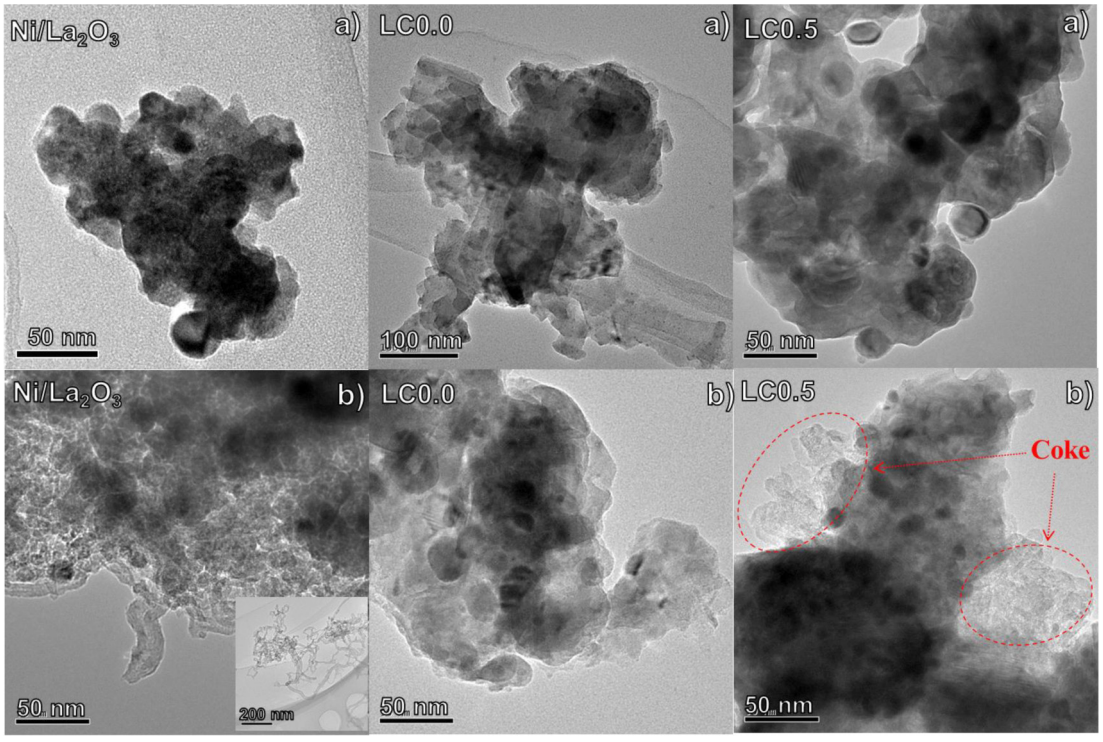

Fig. 7. TEM images of reduced (a) and spent (b) selected catalysts.

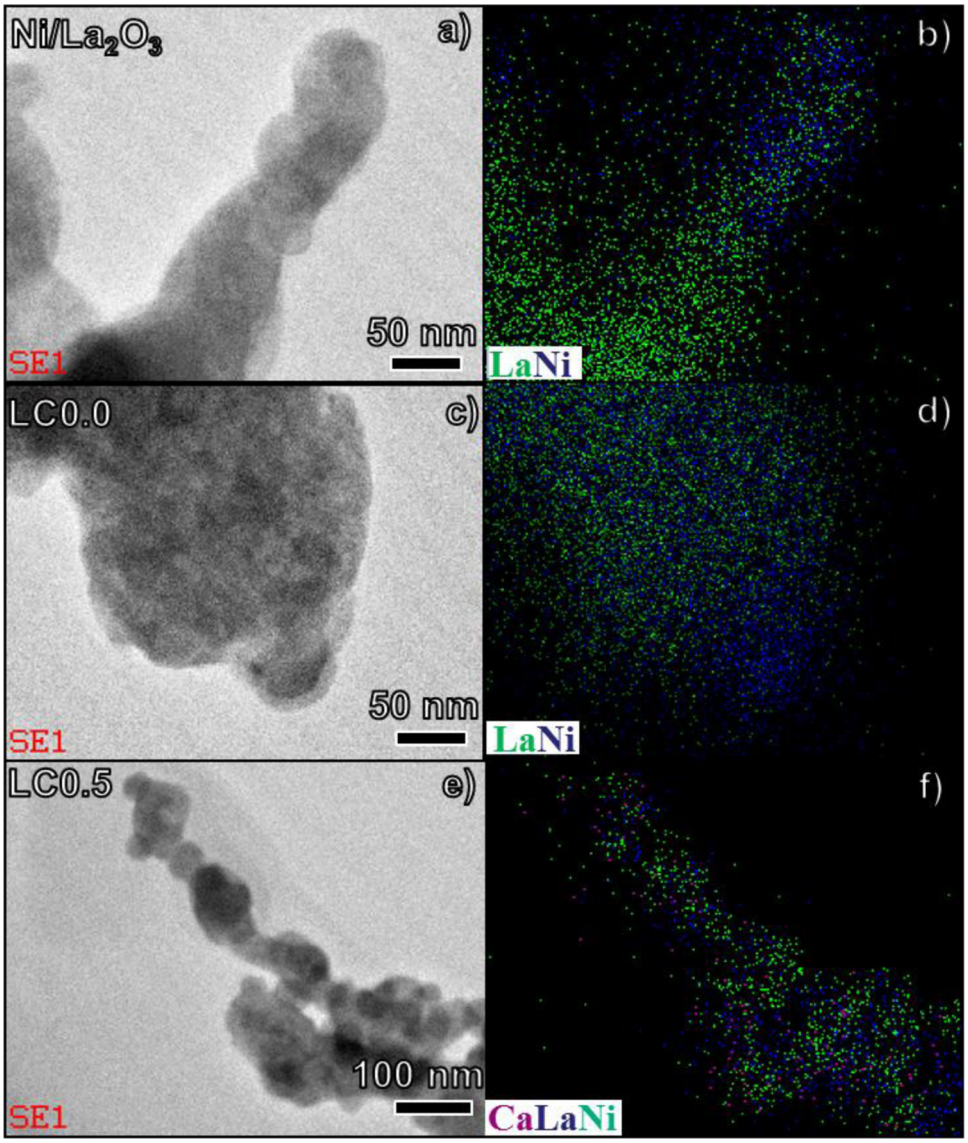

Fig. 8. STEM images and corresponding EDS elemental maps of La, Ni and Ca for reduced Ni/La_2O_3, LC0.0 and LC0.5.

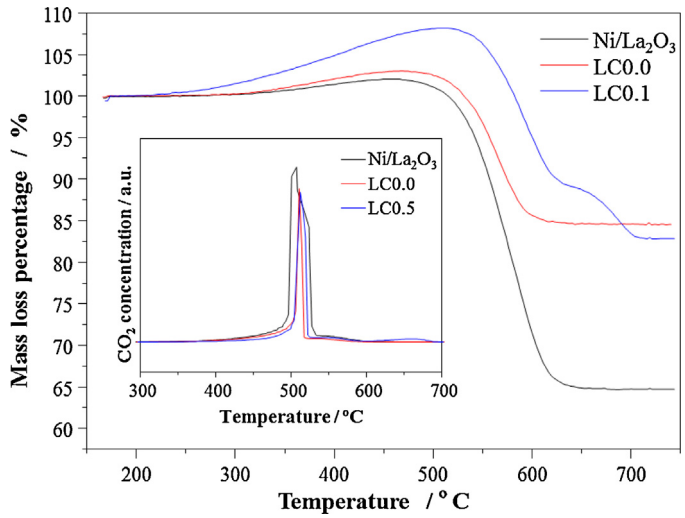

Fig. 9. TGA profiles and TPO results (inset) for spent catalysts.

of olefin species derived from dehydration, dehydrogenation and cyclisation of glycerol [28,32]. Simultaneously, the nickel particle size is closely related to coking, since large nickel particle size is highly favored by coking and dehydration reaction pathway [76–80]. Thus, serious coke deposition and catalyst deactivation was observed on Ni/La_2O_3 catalyst in stability test. Moreover, the MSI is also an important factor to consider when designing steam reforming catalysts to achieve a stable catalytic performance, since a strong MSI may lead to more efficient electron transfer between metal and support [22,31,32]. For example, in Rossetti et al's work [32], strong MSI could account for high glycerol conversion and a sufficient stability, whereas a weak MSI could lead to a strong decrease in the catalytic activity. Though presenting similar metal dispersion with Ni/La_2O_3, LC0.0 exhibits stronger MSI than Ni/La_2O_3. Additionally, the nickel particle size of LC0.0 is the smallest among all the prepared catalysts. Hence, the smallest amount of carbon deposition occurs in LC0.0, together with improved catalytic performance. For LC0.5, the synergetic effect caused by the partial substitution of La by Ca in the perovskite structure produces the highest metal dispersion and the strongest MSI. The sufficient metallic nickel sites, together with the strong MSI, seem

to play a leading role in the stability test of GSR, rather than the large Ni particle as Ni/La_2O_3 contains. Thus, LC0.5 presents the highest H_2 yield and best catalyst stability, and TGA also confirm the existence of a considerable amount of nickel metal in the spent LC0.5. Simultaneously, it should be noticed that spent LC0.5 catalyst contains more deposited carbon than LC0.0, and this may be caused by the larger size of metallic nickel. Additionally, higher activity during steam reforming process might simultaneously cause more deposited carbon on spent catalyst, which was also reported by Atong et al. [72] on $La_{1-x}Ce_xNiO_3$ perovskite-type catalyst for steam reforming of toluene as well as by Sun et al. [81] on Ni–CaO–ZrO_2 catalyst for dry reforming of methane.

4. Conclusions

The $La_{1-x}Ca_xNiO_3$ perovskite-type oxides were synthesized and investigated for GSR. Nickel-based catalysts derived from perovskite-type oxides possessed uniform distribution of Ni and La upon reduction treatment. Therefore, the interfacial area between Ni and oxides was increased and the nickel particles could also be confined by surrounding oxides, which were critical factors for the properties of the reforming catalysts. Accordingly, stronger MSI and smaller Ni metallic particles were observed in $LaNiO_3$, rather than Ni/La_2O_3 catalyst prepared by impregnation method. The partial substitution of La by Ca also showed evident influence on the properties of the perovskite-type oxides, and LC0.5 was the optimized catalyst owing to its strongest MSI and best metal dispersion. Both properties could highly determine the catalytic performance of prepared catalysts in GSR. Additionally, the deactivation of catalysts in GSR was attributed to the coke deposition that covers the active sites. Specifically, smaller Ni particle size and stronger MSI could suppress carbon deposition, and thus improve the catalyst stability in glycerol reforming.

Acknowledgements

We thank Natural Science Foundation of China (21006068, 21222604 and 21206115), the Program for New Century Excellent Talents in University (NCET-10-0611), Specialized Research Fund for the Doctoral Program of Higher Education (20120032110024), the Scientific Research Foundation for the Returned Overseas Chinese Scholars (MoE), Foundation of Peiyang Scholars of Tianjin University, and the Program of Introducing Talents of Discipline to Universities (B06006).

References

[1] B. Katryniok, H. Kimura, E. Skrzynska, J.S. Girardon, P. Fongarland, M. Capron, R. Ducoulombier, N. Mimura, S. Paul, F. Dumeignil, Green Chemistry 13 (2011) 1960–1979.
[2] P.R. d. l. Piscina, N. Homs, Chemical Society Reviews 37 (2008) 2459–2467.
[3] A. Demirbas, Energy Conversion and Management 47 (2006) 2271–2282.
[4] J.C. Serrano-Ruiz, R. Luque, A. Sepulveda-Escribano, Chemical Society Reviews 40 (2011) 5266–5281.
[5] C.H. Zhou, J.N. Beltramini, Y.X. Fan, G.Q. Lu, Chemical Society Reviews 37 (2008) 527–549.
[6] M. Pagliaro, R. Ciriminna, H. Kimura, M. Rossi, C. Della-Pina, Angewandte Chemie International Edition 46 (2007) 4434–4440.
[7] M.L. Dieuzeide, V. Iannibelli, M. Jobbagy, N. Amadeo, International Journal of Hydrogen Energy 37 (2012) 14926–14930.
[8] A. Corma, G. Huber, L. Sauvanaud, P. Oconnor, Journal of Catalysis 257 (2008) 163–171.
[9] J.N. Chheda, G.W. Huber, J.A. Dumesic, Angewandte Chemie International Edition 46 (2007) 7164–7183.
[10] R.R. Soares, D.A. Simonetti, J.A. Dumesic, Angewandte Chemie International Edition in English 45 (2006) 3982–3985.
[11] J. Fermoso, L. He, D. Chen, International Journal of Hydrogen Energy 37 (2012) 14047–14054.
[12] L.V. Mattos, G. Jacobs, B.H. Davis, F.B. Noronha, Chemical Reviews 112 (2012) 4094–4123.
[13] L. He, J.M.S. Parra, E.A. Blekkan, D. Chen, Energy and Environmental Science 3 (2010) 1046–1056.
[14] S.M. Kim, S.I. Woo, ChemSusChem 5 (2012) 1513–1522.
[15] D. Simonetti, E. Kunkes, J. Dumesic, Journal of Catalysis 247 (2007) 298–306.
[16] T. Valliyappan, N.N. Bakhshi, A.K. Dalai, Bioresource Technology 99 (2008) 4476–4483.
[17] P. Dauenhauer, J. Salge, L. Schmidt, Journal of Catalysis 244 (2006) 238–247.
[18] D.C. Rennard, J.S. Kruger, B.C. Michael, L.D. Schmidt, Industrial and Engineering Chemistry Research 49 (2010) 8424–8432.
[19] G.W. Huber, J.W. Shabaker, J.A. Dumesic, Science 300 (2003) 2075–2077.
[20] J.W. Shabaker, G.W. Huber, J.A. Dumesic, Journal of Catalysis 222 (2004) 180–191.
[21] Y. Cui, V. Galvita, L. Rihko-Struckmann, H. Lorenz, K. Sundmacher, Applied Catalysis B: Environmental 90 (2009) 29–37.
[22] A. Iriondo, V.L. Barrio, J.F. Cambra, P.L. Arias, M.B. Guemez, M.C. Sanchez-Sanchez, R.M. Navarro, J.L.G. Fierro, International Journal of Hydrogen Energy 35 (2010) 11622–11633.
[23] X. Wang, N. Wang, M. Li, S. Li, S. Wang, X. Ma, International Journal of Hydrogen Energy 35 (2010) 10252–10256.
[24] I. Iliuta, H.R. Radfarnia, M.C. Iliuta, AIChE Journal 59 (2013) 2105–2118.
[25] P.D. Vaidya, A.E. Rodrigues, Chemical Engineering and Technology 32 (2009) 1463–1469.
[26] S. Adhikari, S.D. Fernando, A. Haryanto, Energy Conversion and Management 50 (2009) 2600–2604.
[27] Y.-C. Lin, International Journal of Hydrogen Energy 38 (2013) 2678–2700.
[28] F. Pompeo, G. Santori, N.N. Nichio, International Journal of Hydrogen Energy 35 (2010) 8912–8920.
[29] C. Zhang, P. Zhang, S. Li, G. Wu, X. Ma, J. Gong, Physical Chemistry Chemical Physics 14 (2012) 3295–3298.
[30] L.F. Bobadilla, A. Álvarez, M.I. Domínguez, F. Romero-Sarria, M.A. Centeno, M. Montes, J.A. Odriozola, Applied Catalysis B: Environmental 123–124 (2012) 379–390.
[31] V. Nichele, M. Signoretto, F. Menegazzo, A. Gallo, V. Dal Santo, G. Cruciani, G. Cerrato, Applied Catalysis B: Environmental 111–112 (2012) 225–232.
[32] I. Rossetti, A. Gallo, V. Dal Santo, C.L. Bianchi, V. Nichele, M. Signoretto, E. Finocchio, G. Ramis, A. Di Michele, ChemCatChem 5 (2013) 294–306.
[33] C. Zhang, H. Yue, Z. Huang, S. Li, G. Wu, X. Ma, J. Gong, ACS Sustainable Chemistry and Engineering 1 (2013) 161–173.
[34] S. Li, C. Zhang, Z. Huang, G. Wu, J. Gong, Chemical Communications 49 (2013) 4226–4228.
[35] G. Wu, C. Zhang, S. Li, Z. Huang, S. Yan, S. Wang, X. Ma, J. Gong, Energy and Environmental Science 5 (2012) 8942–8949.
[36] S.M. de Lima, A.M. da Silva, L.O.O. da Costa, J.M. Assaf, L.V. Mattos, R. Sarkari, A. Venugopal, F.B. Noronha, Applied Catalysis B: Environmental 121–122 (2012) 1–9.
[37] K. Urasaki, Y. Sekine, S. Kawabe, E. Kikuchi, M. Matsukata, Applied Catalysis A: General 286 (2005) 23–29.
[38] A. Glisenti, A. Galenda, M.M. Natile, Applied Catalysis A: General 453 (2013) 102–112.
[39] S.Q. Chen, H. Wang, Y. Liu, International Journal of Hydrogen Energy 34 (2009) 7995–8005.
[40] B.P. Barbero, J.A. Gamboa, L.E. Cadús, Applied Catalysis B: Environmental 65 (2006) 21–30.
[41] J.R. Mawdsley, T.R. Krause, Applied Catalysis A: General 334 (2008) 311–320.
[42] I. Rossetti, L. Forni, Applied Catalysis B: Environmental 33 (2001) 345–352.
[43] G. Valderrama, M.R. Goldwasser, C.U. d. Navarro, J.M. Tatibouët, J. Barrault, C. Batiot-Dupeyrat, F. Martínez, Catalysis Today 107–108 (2005) 785–791.
[44] G.S. Gallego, F. Mondragón, J. Barrault, J.-M. Tatibouët, C. Batiot-Dupeyrat, Applied Catalysis A: General 311 (2006) 164–171.
[45] R.M. Navarro, M.C. Alvarez-Galvan, J.A. Villoria, I.D. González-Jiménez, F. Rosa, J.L.G. Fierro, Applied Catalysis B: Environmental 73 (2007) 247–258.
[46] C. Batiot-Dupeyrat, G.A.S. Gallego, F. Mondragon, J. Barrault, J.-M. Tatibouët, Catalysis Today 107–108 (2005) 474–480.
[47] G.S. Gallego, C. Batiot-Dupeyrat, J. Barrault, E. Florez, F. Mondragón, Applied Catalysis A: General 334 (2008) 251–258.
[48] R. Pereñíguez, V.M. González-DelaCruz, J.P. Holgado, A. Caballero, Applied Catalysis B: Environmental 93 (2010) 346–353.
[49] S. de Lima, M. Peña, J. Fierro, J. Assaf, Catalysis Letters 124 (2008) 195–203.
[50] M.R. Goldwasser, M.E. Rivas, E. Pietri, M.J. Pérez-Zurita, M.L. Cubeiro, L. Gingembre, L. Leclercq, G. Leclercq, Applied Catalysis A: General 255 (2003) 45–57.
[51] Z.L. Zhang, X.E. Verykios, Catalysis Today 21 (1994) 589–595.
[52] C.K.S. Choong, Z. Zhong, L. Huang, Z. Wang, T.P. Ang, A. Borgna, J. Lin, L. Hong, L. Chen, Applied Catalysis A: General 407 (2011) 145–154.
[53] G. Yang, H. Yu, X. Huang, F. Peng, H. Wang, Applied Catalysis B: Environmental 127 (2012) 89–98.
[54] S.M. Lima, J.M. Assaf, M.A. Peña, J.L.G. Fierro, Applied Catalysis A: General 311 (2006) 94–104.
[55] G. Sierra Gallego, F. Mondragón, J.-M. Tatibouët, J. Barrault, C. Batiot-Dupeyrat, Catalysis Today 133–135 (2008) 200–209.
[56] A. Khalesi, H.R. Arandiyan, M. Parvari, Chinese Journal of Catalysis 29 (2008) 960–968.
[57] V.V. Thyssen, T.A. Maia, E.M. Assaf, Fuel 105 (2013) 358–363.
[58] S. Li, C. Zhang, P. Zhang, G. Wu, X. Ma, J. Gong, Physical Chemistry Chemical Physics 14 (2012) 4066–4069.

[59] C. Zhang, S. Li, M. Li, S. Wang, X. Ma, J. Gong, AIChE Journal 58 (2012) 516–525.
[60] S.M. de Lima, A.M. da Silva, L.O.O. da Costa, J.M. Assaf, G. Jacobs, B.H. Davis, L.V. Mattos, F.B. Noronha, Applied Catalysis A: General 377 (2010) 181–190.
[61] S. Adhikari, S. Fernando, A. Haryanto, Energy and Fuels 21 (2007) 2306–2310.
[62] A. Gallo, C. Pirovano, P. Ferrini, M. Marelli, R. Psaro, S. Santangelo, G. Faggio, V. Dal Santo, Applied Catalysis B: Environmental 121–122 (2012) 40–49.
[63] B. Zhang, X. Tang, Y. Li, Y. Xu, W. Shen, International Journal of Hydrogen Energy 32 (2007) 2367–2373.
[64] E.L. Kunkes, R.R. Soares, D.A. Simonetti, J.A. Dumesic, Applied Catalysis B: Environmental 90 (2009) 693–698.
[65] G. Wu, C. Zhang, S. Li, Z. Han, T. Wang, X. Ma, J. Gong, ACS Sustainable Chemistry and Engineering (2013), http://dx.doi.org/10.1021/sc400123f.
[66] H. Chen, Y. Ding, N.T. Cong, B. Dou, V. Dupont, M. Ghadiri, P.T. Williams, Renewable Energy 36 (2011) 779–788.
[67] C.K. Cheng, S.Y. Foo, A.A. Adesina, Industrial and Engineering Chemistry Research 49 (2010) 10804–10817.
[68] T. Hirai, N.-o. Ikenaga, T. Miyake, T. Suzuki, Energy and Fuels 19 (2005) 1761–1762.
[69] S. Adhikari, S.D. Fernando, S.D.F. To, R.M. Bricka, P.H. Steele, A. Haryanto, Energy and Fuels 22 (2008) 1220–1226.
[70] A. Iriondo, V.L. Barrio, J.F. Cambra, P.L. Arias, M.B. Güemez, R.M. Navarro, M.C. Sánchez-Sánchez, J.L.G. Fierro, Topics in Catalysis 49 (2008) 46–58.
[71] N. Mota, M.C. Alvarez-Galván, R.M. Navarro, S.M. Al-Zahrani, A. Goguet, H. Daly, W. Zhang, A. Trunschke, R. Schlögl, J.L.G. Fierro, Applied Catalysis B: Environmental 113–114 (2012) 271–280.
[72] K. Soongprasit, D. Aht-Ong, V. Sricharoenchaikul, D. Atong, Current Applied Physics 12 (Supplement 2) (2012) S80–S88.
[73] P.-Z. Li, K. Aranishi, Q. Xu, Chemical Communications 48 (2012) 3173–3175.
[74] W.-T. Zheng, K.-Q. Sun, H.-M. Liu, Y. Liang, B.-Q. Xu, International Journal of Hydrogen Energy 37 (2012) 11735–11747.
[75] V. Chiodo, S. Freni, A. Galvagno, N. Mondello, F. Frusteri, Applied Catalysis A: General 381 (2010) 1–7.
[76] A.J. Vizcaíno, A. Carrero, J.A. Calles, Catalysis Today 146 (2009) 63–70.
[77] K.O. Christensen, D. Chen, R. Lødeng, A. Holmen, Applied Catalysis A: General 314 (2006) 9–22.
[78] G. Centi, S. Perathoner, Catalysis Today 148 (2009) 191–205.
[79] D. Chen, K.O. Christensen, E. Ochoa-Fernández, Z. Yu, B. Tøtdal, N. Latorre, A. Monzón, A. Holmen, Journal of Catalysis 229 (2005) 82–96.
[80] V.M. Gonzalez-DelaCruz, J.P. Holgado, R. Pereñíguez, A. Caballero, Journal of Catalysis 257 (2008) 307–314.
[81] N. Sun, X. Wen, F. Wang, W. Peng, N. Zhao, F. Xiao, W. Wei, Y. Sun, J. Kang, Applied Surface Science 257 (2011) 9169–9176.